

NON-UNIFORM FREE-FREE ABSORPTION IN THE GPS RADIO GALAXY 0108+388

J. M. MARR¹, G. B. TAYLOR², AND F. CRAWFORD³

Accepted by the Astrophysical Journal

ABSTRACT

We have observed the canonical gigahertz-peaked spectrum source 0108+388 with the VLBA at a range of frequencies above and below the spectral peak. The activity that dominates the radio emission from 0108+388, which is also classified as a Compact Symmetric Object, is thought to be less than 1000 years old. We present strong evidence that the spectral turnover in 0108+388 results from free-free absorption by non-uniform gas, possibly in the form of a disk in the central tens of parsecs.

Subject headings: galaxies: active — galaxies: nuclei — galaxies: individual (0108+388) — radio continuum: galaxies — galaxies: ISM — methods: data analysis

1. INTRODUCTION

The radio source 0108+388 (RA=01^h11^m37^s.32, Dec=39°06′28″.1 (J2000), $z=0.699$) is an example of a class of extragalactic radio source referred to as Gigahertz-Peaked Spectrum (or GPS) sources. GPS sources, which are discussed at length in a thorough review by O’Dea (1998), are characterized by large radio luminosities, compact structure, and spectra that turn over at Gigahertz frequencies with steep spectra on either side of the peak (O’Dea, Baum, & Stanghellini 1991; O’Dea 1998). The steep slope at high frequencies is generally accepted to be due to synchrotron losses, but there are two main competing theories for the cause of the low frequency turnover. Either the lower frequency radio emission is absorbed by ionized gas in the line of sight in the host galaxies, with conditions comparable to that of emission-line regions in active galaxies (van Breugel, Heckman, & Miley 1984, Bicknell, Dopita, & O’Dea 1997; Kameno et al. 2000), or the nuclei of these galaxies have exceptionally large magnetic fields, causing synchrotron self-absorption at GHz frequencies (Hodges, Mutel, & Phillips 1984; Mutel, Hodges, & Phillips 1985; O’Dea et al. 1991; Readhead et al. 1996; de Vries, Barthel, & O’Dea 1997; Snellen et al. 2000). Absorption by induced Compton scattering in combination with free-free absorption has also been proposed by Kuncic, Bicknell, & Dopita (1998).

As GPS sources have been studied in more detail since the discovery of a large population of such sources in the 1980’s (Gopal-Krishna, Patnaik, & Steppe 1983, Spoelstra, Patnaik, & Gopal-Krishna 1985), it has become apparent that they constitute a diverse group, with morphological and spectral variances. The object we discuss here, 0108+388, is a canonical case of a morphological group referred to by Wilkinson et al. (1994) as compact symmetric objects (or CSO’s), which have small (< 1 kpc) symmetric radio emission structure. Multi-epoch VLBI observations of a number of CSO’s have revealed expansion rates that imply ages of the order of 1000 years (Owsianik, Conway, & Polatidis 1998; Owsianik & Conway 1998; Taylor et al. 2000), supporting the earlier hypothesis that CSO’s

are precursors to the young classical double radio galaxies (Phillips & Mutel 1982; Carvalho 1985; Readhead et al. 1996). VLBI observations of 0108+388 by Owsianik et al. (1998) and by Taylor et al. (2000) infer apparent separation speeds of the outer components of $0.197 \pm 0.026 h^{-1} c$ and $0.24 \pm 0.04 h^{-1} c$, respectively, from which these authors derive kinematic ages of just 367 ± 48 yr and 310 ± 70 yr, respectively. This is the youngest age yet measured for a radio galaxy. However, with VLA and WSRT observations of 0108+388 Baum et al. (1990) detected emission 20 arcsec ($78 h^{-1}$ kpc) from the core, casting an apparent contradiction to the young classical double radio galaxy model. Baum et al. propose that either the activity in 0108+388 is recurrent or has recently been smothered by infalling gas.

High resolution imaging of 0108+388 was first undertaken at 5 GHz as part of the PR VLBI survey (Pearson & Readhead 1988) and found to have a simple double structure. Conway et al. (1994) and Taylor, Readhead, & Pearson (1996) made more sensitive and higher resolution images at higher frequencies that revealed a steeply inverted core component connected to both outer components by a faint chain of components. Overall, 0108+388 has an ‘S’ symmetry that is relatively common among CSOs (Readhead et al. 1996).

The spectrum of the total radio emission from the compact structure in 0108+388 was analyzed by Baum et al. (1990). They measured a spectral index below the turnover that was steep and roughly constant, in conflict with the exponential turnover expected from free-free absorption. However, their observed spectrum is the total from several components in the source. An exponential turnover in the free-free absorption case will apply only if the absorbing medium uniformly covers the entire radio source. We report here on a set of VLBA observations designed to study the absorption at each point in the map. We have observed 0108+388 with the VLBA at five frequencies: two above the turnover, two below the turnover, and one at the turnover frequency itself. The maps made with these observations reveal the morphology of the radio emission from 0108+388 and how it is obscured by

¹Union College, Schenectady, NY 12308, USA; marrj@union.edu

²NRAO, Socorro, NM 87801, USA; gtaylor@nrao.edu

³MIT, Cambridge, MA 02139, USA; crawford@space.mit.edu

absorption. We find that the spectra of 0108+388 at all positions in our maps are consistent with free-free absorption. Additionally, our maps reveal that the absorption is non-uniform and is suggestive of an edge-on disk centered on the core. Other evidence for a large amount of thermal gas along the line of sight to the core of 0108+388 has been reported by Carilli et al. (1998), who measured significant absorption by HI, and by Cawthorne et al. (1993), who find no measurable polarization of the radio emission. The existence of a circumnuclear gas disk, with likely instabilities, could also be the source of intermittent fueling of the central engine and explain the recent onset of activity along with the past activity.

2. OBSERVATIONS AND MAPPING

We observed 0108+388 with the Very Long Baseline Array (VLBA)⁴ at 8.417, 4.983, 2.267, and 1.663 GHz on 1996 June 24 and at 15.359 and 8.415 GHz on 1997 February 03. In the 1996 observations, the source signal was recorded at each station for a total of 100 to 112.5 minutes at each frequency, with an integration time of 2 seconds. In the 1997 observations a total of 330 minutes on source was obtained at both 8.415 and 15.359 GHz. The on-source scans at all frequencies and both epochs were spread across a wide range in hour angle in order to obtain good u - v coverage.

Fringe fitting was performed with AIPS using the small and bright source J0136+478 as a fringe calibrator. In the fringe searches we generally used solution intervals of 3 minutes, moderately large delay and rate windows (100 ns and 40 mHz), and a minimum signal-to-noise ratio of 7. Good solutions were generally found at small and stable delays and rates. We applied *a priori* amplitude calibration, also with AIPS, using the system temperatures and gains measured by the NRAO staff. We assume that the amplitude calibration is accurate to within 5%. The detected flux densities on the shortest baselines were all greater than 92% of previously reported flux densities from low resolution observations (Baum et al. 1990; O’Dea et al. 1990; UMRAO database).

Editing, modelfitting, and mapping were done using Difmap (Shepherd, Pearson, & Taylor 1994, 1995; Shepherd 1997). Starting with the 1997 15-GHz data, we used an initial model of seven elliptical gaussian components, based on the appearance of the clean map made by Taylor et al. (1996). The model parameters were then allowed to vary to yield a best rms-fit in the u - v plane to the self-calibrated data. We found best-fit models for each data set independently except that we checked for general consistency in the positions of components at all frequencies. The final model for each data set fit the self-calibrated data with an rms difference of around 1σ .

We fed the best-fit models as input models for Hybrid CLEAN (Readhead & Wilkinson 1978), which we used to obtain our final image maps. We initially used small CLEAN boxes that barely encompassed the apparent emission in the dirty map. After 100 CLEAN components were selected, with a gain of just 0.05, we increased the sizes of the CLEAN boxes while always staying marginally larger than the area of the apparent flux

in the residual map. We excluded apparent spurious features from the CLEAN boxes the first few cycles of self-cal and CLEAN. CLEANing was generally stopped a few clean components before the first negative component. The maps were of sufficiently high quality that all the detected flux on the shortest baselines was collected in the CLEANing by this point. We did not apply amplitude self-calibration until the model agreed with the data with an rms difference less than 1.5σ . The final clean component models fit the data to better than 1.0σ . The noise in the maps range from 0.2 mJy/beam in the 8.4-GHz maps to 0.7 mJy/beam in the low frequency maps, yielding signal-to-noise ratios from 300 to over 1000.

We also made spectral index maps between neighboring frequency bands using the AIPS task COMB. We first edited the data at each frequency, removing the larger u - v spacings from the higher frequency data and the smaller u - v spacings from the lower frequency data, and remapped in Difmap. The maps at the two frequencies were convolved with identical clean beams. In this way, we produced spectral index maps between 1.7 and 2.3 GHz, between 2.3 and 5.0 GHz, between 5.0 and 8.4 GHz from the 1996 June observations, and between 8.4 and 15.4 GHz from the 1997 February observations. Since moderate percentage errors in the observed maps propagate to large errors in the spectral index, we masked the spectral index maps where the signal in either clean map was less than 10σ .

Since the observations were not phase-referenced to a nearby calibrator, no absolute position information is available for each map. Each map, therefore, can be arbitrarily shifted in RA and Dec, and so the correct alignment of the maps is not known *a priori*. This is a critical issue in making spectral index maps. If the maps are misaligned, extremely large and extremely small spectral indices will be inferred, particularly at the edges of the emission regions. At the higher frequencies (from 5.0 to 15.4 GHz) the relative positions of the component peaks were consistent such that they could be used to determine the alignments of the maps. The resultant spectral index maps were quite reasonable in that they did not show surprisingly large spectral indices at the edges or sides of the features. At the lower frequencies, however, the separations of the centroids of the components varied. For these spectral index maps, we chose alignments that yielded the minimum magnitudes of the extreme spectral indices. Additionally, since the flux-density distribution in the maps appears relatively symmetric, especially in the lower resolution maps, we also checked the alignment of the maps by examining the spectral index map and watching for dipolar distributions of inferred spectral indices. We successfully found relative alignments that minimized the spectral index extremes and that yielded roughly symmetrical spectral indices.

3. RESULTS

The CLEAN maps for each observation are shown in Figure 1. As noted by previous investigators of this source (Pearson & Readhead 1988; Conway et al. 1994; Taylor et al. 1996; Owsianik & Conway 1998; Owsianik et al. 1998) the intensity distribution of the source at all frequencies

⁴The VLBA is operated by the National Radio Astronomy Observatory, which is a facility of the National Science Foundation operated under cooperative agreement by Associated Universities, Inc.

consistently involves two major components. Following the notation of Taylor et al. (1996), we refer to these components as C1 (in the southwest) and C7 (in the northeast). At the higher frequencies (15.4 and 8.4 GHz) we obtained models with a total of seven components, while at the three lower frequencies we could reasonably fit only four components, due to blending of the smaller components.

3.1. Spectral Index Maps

The spectral index maps are shown in Figure 2. The uncertainties in the inferred spectral indices, calculated by propagating both uncertainties in amplitude calibration and the map noise, are listed in Table 1.

The spectral index map between the two highest frequencies shows that the two major components have steeply declining spectra, with spectral indices $\alpha \approx -1.0$, where $F_\nu \propto \nu^\alpha$. A small region between the two major components, centered on component C3, in the notation of Taylor et al. (1996), has an inverted spectrum with α getting as large as +1.8, suggesting that the core of this active galaxy is located here, as previously noted by Taylor et al. (1996).

Between 8.4 and 5.0 GHz, the spectra of the regions containing the major components are generally flatter than between 15.4 and 8.4 GHz, although the spectra get steeper towards the outer edges. At 5.0 GHz the core region has small flux densities, so most of this central region is masked in the spectral index map.

Between 5.0 and 2.3 GHz, the spectral index map shows that the spectra of all but the easternmost and westernmost edges are inverted ($\alpha > 0$). At the very edges of the eastern and western extremes the spectral indices are still seen to get as low as -0.7 . The region with inverted spectra appears to run across the map in the north-south direction, but with the steepest parts located in two areas north and south of the core at the edge of the mapped region. The core is not detected at these frequencies due to its low luminosities and steeply inverted spectrum.

Between 2.3 and 1.7 GHz, the spectral index map looks very similar to the 2.3-5.0 GHz spectral index map, except that all the spectral indices across the entire map are larger and the region of inverted spectra encompasses almost the entire source. The two areas of the steepest inverted spectra are more evident and appear even more symmetrical about the core.

3.2. Free-free Absorption Model

As clearly shown in Figure 2 the turnover of the composite spectrum of 0108+388 at 5.0 GHz results from the majority of the source, including the two brightest components of the source, turning over at this frequency. This is in conflict with the expectations for synchrotron self-absorption, in which the small regions with the largest magnetic fields and electron densities would turn over at higher frequencies. The nature of the turnover in 0108+388, however, is consistent with the absorption being due to free-free absorption by a foreground screen of ionized gas. Additionally, the peak spectral index between 2.3 and 1.7 GHz, even at the moderately low resolution of the map in Figure 2d, is 3.2 ± 0.5 . This is larger than the maximum spectral index allowed by classical self-absorption models, although it can be fit to synchrotron

self-absorption with special physical conditions (see, e.g., de Kool & Begelman 1989).

The spectral index maps also suggest the shape and structure of the absorbing gas, which appears to be extended north-south with two density peaks on either side of the center. This is suggestive of an edge-on disk centered on the core of the galaxy. However, the spectral index only measures the ratio of the flux at two frequencies and does not directly indicate the densities of the absorbing gas. To directly map the absorbing gas we made opacity maps, which we discuss in the following section.

3.3. Opacity Maps

The creation of opacity maps involves comparison of maps at all the observed frequencies (as described below). For this purpose, all data sets were re-mapped with the same resolution. Two methods were used. First, we simply convolved all clean maps with the same beam as the clean beam at 1.7 GHz. This approach is flawed, in general, because the different frequency observations (with the same array) probe structures of different sizes, and so even with the same clean beam different features are being compared. As a second approach we edited all data sets to have the same minimum and maximum u - v distances; all data sets were flagged to have the same maximum u - v distance as in the 1.7-GHz data set and the same minimum u - v distance as in the 15.4-GHz data. These truncated data sets had aspect ratios of only 9.0 and so this method could result in the maps missing much of the structure, both on large and on small scales. For example, the detected flux densities on the remaining shortest baselines at 2.7 and 1.3 GHz were 87% and 78%, respectively, of those in the full data sets. Interestingly, there were no significant differences in the final maps made with these two methods and the maps looked very much like the 2.3 and 1.7 GHz clean maps in Figure 1. Furthermore the signal to noise ratios in the final maps made from the edited data sets were, in general, higher than in the clean maps from the untruncated data sets, especially at the mid-frequencies; this resulted primarily because the editing removed the data at the extremes in the u - v plane, which corresponds to where the density of data is lowest. The high fidelity of these maps resulted from the simplicity of the structure of this source at these low frequencies. The clean maps made from the truncated data sets are shown in Figure 3.

To infer optical depths we need flux-density maps in the absence of the absorption. We obtain such maps by extrapolating the spectra at the higher frequencies. Since the spectra of the major components between 15.4 and 8.4 GHz are steeply declining with increasing frequency, the absorption at these frequencies is small and so the flux densities at these frequencies provide a close approximation of the unabsorbed emission spectrum. If $\alpha_{15-8}(x, y)$ is the spectral index between 15.4 and 8.4 GHz at some position (x, y) in the map, and $F_{8.4\text{GHz}}(x, y)$ is the flux density at 8.4 GHz at this position, then the approximate unabsorbed flux density at 2.3 GHz is

$$\text{Unabsorbed } F_{2.3\text{GHz}}(x, y) = F_{8.4\text{GHz}}(x, y) \left[\frac{2.3 \text{ GHz}}{8.4 \text{ GHz}} \right]^{\alpha_{15-8}(x, y)}. \quad (1)$$

We then obtain an approximation of the optical depth at 2.3 GHz at each point in the map by

$$\tau(x, y) = -\ln(\text{observed } F_\nu(x, y)) + \ln(\text{unabsorbed } F_\nu(x, y)). \quad (2)$$

However, since the optical depths at 8.4 and 15.4 GHz are not really zero, the extrapolation of the spectrum produces a small error. We improve the inferred optical depths by iterating the procedure; we use the inferred optical depths at 2.3 GHz to infer the optical depths at 8.4 and 15.4 GHz, assuming free-free absorption. We then correct the 8.4 and 15.4 GHz maps for the non-zero optical depths, yielding maps of the unabsorbed flux-densities at these frequencies. We then used these modified maps to recreate the 15.4-8.4 GHz spectral index map and the unabsorbed 1.7 and 2.3 GHz flux density maps, which we used, in turn, to create improved opacity maps.

The opacity maps were made from the maps shown in Figure 3 by using a number of steps of the AIPS task COMB which reproduced the math discussed in the previous paragraph. The low-frequency flux densities (at 5.0, 2.3, and 1.7 GHz) were extrapolated from the 8.4-GHz flux densities of the same epoch (1996 June) while the spectral indices between 15.4 GHz and 8.4 GHz ($\alpha_{15-8}(x, y)$) were calculated using the 8.4-GHz data of the same epoch (1997 February) as the 15.4-GHz data. The resultant opacity maps at 2.3 and 1.7 GHz are shown in Figure 4. The uncertainties in the optical depths are primarily due to the 5% uncertainty in amplitude calibration, which yields a constant uncertainty across each map. The calculated uncertainties due to amplitude calibration errors are listed in Table 2. The opacity maps at 5.0, 2.3, and 1.7 GHz are nearly identical, except that the optical depths are larger at lower frequencies, as expected. The optical depths at 5.0 GHz are small, relative to the uncertainty, and so the 5.0-GHz opacity map is dominated by noise and so is not displayed in Figure 4. The opacity maps are nearly identical in appearance. These maps also indeed show that the maximum absorption occurs at two points north and south of the center and that the optical depth decreases in the direction perpendicular to the line connecting the optical depth peaks.

At each point in the map, we have a measure of the optical depth at three different frequencies, and so we can check whether free-free absorption fits the observed spectra everywhere. The optical depth of free-free absorption, in a simple single-component model, depends on frequency according to

$$\tau_\nu = 0.08235 \nu^{-2.1} \int T_e^{-1.35} N_e^2 dl,$$

where $\nu < 10$ GHz and is given in GHz, N_e is in units of cm^{-3} , and L is in pc (Mezger & Henderson 1967). Assuming this model, we can remove the frequency dependence in our opacity maps, and check for consistency between the data at different frequencies, by multiplying the optical depths in the maps of Figure 4 by $\nu^{2.1}$ (using the AIPS task COMB). If each position in these maps has a single free-free absorption component, then the resultant images will display maps of the value $0.08235 \int T_e^{-1.35} N_e^2 dl$. These maps are shown in Figure 5 (again, because of the large uncertainty relative to calculated values we do not display the map at 5.0 GHz). The uncertainties in these values,

calculated by propagating through just the amplitude calibration errors, are listed in Table 2 (the total uncertainties actually include errors due to map noise, which are significant only near the edges of the source). The maps in Figure 5 are essentially identical. In Figure 6 we display the difference between the two maps in Figure 5 divided by the total uncertainty, due to both amplitude calibration errors and map noise. The contours displayed in Figure 6 represent difference values of -0.5 , 0.5 , 1 , and 2 times the calculated uncertainty. The differences are typically $\approx 1.0\sigma$ across the map, with a mean of 1.1σ , and get as large as 2.1σ only near the southwest edge. The rms value in Figure 6, and hence the rms deviation between the maps in Figure 5, is 1.26σ .

As is evident in Figures 4 and 5, the optical depth is not uniform over the map and most likely varies on scales smaller than the resolution of these maps. Therefore, one should not expect the single-component free-free absorption model to perfectly fit the spectra at each point in our moderately low resolution maps. Therefore, a reduced χ^2 value for the agreement between this simple model and our data across our entire map of just 1.26 is striking and strongly supports the premise that free-free absorption is at work. Only a mild level of complexity, such as a variable electron density across our synthesized beam, would be needed to produce a fit with an rms deviation of less than 1σ .

3.4. Individual Spectra

As an additional test, one can fit a free-free absorption model to individual spectra. By stacking the maps in Figure 3, with the same alignments that we used to make the opacity maps, we can obtain individual spectra at each location. However, as we discussed in the previous section, one should expect that the optical depth varies on scales below the low resolution of the maps in Figure 3. One should not, therefore, expect the precise fitting of a single-component free-free absorption model to the observed spectra to produce a perfect fit.

In Figure 7, we display the spectra at the locations of the peaks in emission at 5.0 GHz. To correct for any flux variations in the source between our two observation epochs the flux densities at 15.4 GHz in our 1997 observation were multiplied by a scale factor of 0.97, which is the ratio of the 8.4-GHz flux densities in 1996 to that in 1997. The displayed error bars correspond to the total uncertainty in the measured flux densities, due to both the 5% amplitude calibration uncertainty and the rms in the map flux densities.

Overlaid on the observed spectra in Figure 7 are best-fit curves for single-component models of free-free absorption in the foreground of optically thin synchrotron emission sources. The curves in Figure 4 are given by $F_\nu = F_o(\nu/1.5359\text{GHz})^\alpha \exp(-EMT/\nu^{2.1})$. Since our goal is to determine the cause of the absorption at low frequencies, we kept F_o relatively fixed to ensure that the curve passes through the measured 15.4-GHz flux density. Variation in EMT , though, causes slight changes in the model 15.4-GHz flux density, so we needed to allow F_o to vary a little, as EMT varied, to ensure that the flux-density at 15.4 GHz matched the observed value. We, therefore, had two free parameters. The values of these

parameters in the best fit curves are listed in Table 3. Although the curves appear by visual inspection to fit the data well, the reduced χ^2 of the fits, listed in Table 3, are quite large. Almost the entire contribution to these large χ^2 values are in the disagreements at 2.3 and 1.7 GHz, where the slopes of the curves are very steep and small adjustments in the model parameters yield large differences in the curve values. However, a slightly more complex model, such as an electron density that varies by a factor of two on scales below the map resolution, yields nearly perfect fits to the data. We, therefore, find that the observed spectra at these two positions are consistent with a reasonable free-free absorption model.

4. DISCUSSION

4.1. Disk of Ionized Gas

The maps in Figure 5, which show the morphology of the quantity $0.08235 \int T_e^{-1.35} N_e^2 dl$ projected onto the sky plane, show that the absorbing medium is elongated north-south and is concentrated in two spots symmetrical about the core. In Figure 8 we display the 1.7-GHz map from Figure 5 in contours overlaid on a grey-scale plot of the 15.4-GHz clean map from Figure 3. Even with the large clean beam of these maps, the denser regions of the absorbing medium are clearly shown to be located to the sides of the radio emission structure. Such a morphology in optical depth is often symptomatic of a disk centered on the core. If this is indeed a disk, it is roughly perpendicular to the jet axis. One must keep in mind that this medium is probed in our maps only through its absorption of the radio emission from the jet, and so the medium can, and most likely does, extend well beyond the regions indicated in our maps. Additionally, the absorption is caused only by ionized gas and any such disk is most likely to have a large neutral component that is far more extensive. In fact, the observations of Carilli et al. (1998) indicate that a large amount of neutral gas does in fact exist in this galaxy.

In interpreting the morphology of the opacity maps, one must keep in mind that these maps were made with a resolution of 4.4 mas in the North-South direction and 3 mas in the East-West direction. For example, the peaks in optical depth in Figure 4 appear to be located where there is no detectable emission at 15.4 GHz in the high resolution map of Figure 1a. However, since in the process with which we made the opacity maps the input maps were masked where the signal was below 10σ , this doesn't seem possible. The reason that we appear to detect absorption far from the radio emission structure seen in Figure 1a is because of the low resolution of the opacity maps; the 15.4-GHz map of Figure 3a was used in making the opacity maps, not Figure 1a. If we were able to make opacity maps at the resolution of Figure 1a, we would find the optical depth peaks to occur somewhere at the edges of the 15.4-GHz emission. In the opacity maps of Figure 4, the precision of the position information is given by the width of the clean beam, and so a true location of the optical depth peaks 1 mas away from the apparent location is reasonable. The morphological information in our opacity maps of which we can be sure is that indicated in Figure 8, i.e. that the peaks in the optical depth are offset from the peaks in the radio emission. In order for the optical depth peaks to

appear at the edges of our opacity maps, the true optical depth structure must have a similar gradient.

The peaks in optical depth are located about 10 ± 4.4 mas apart. Therefore, if this is indicative of a disk, then the disk appears to have an inner radius of about 5 ± 2.2 mas. With a redshift of 0.699 and a Hubble constant of $100 h \text{ km s}^{-1} \text{ Mpc}^{-1}$, this corresponds to an inner radius of $\approx 50 \pm 20 h^{-1} \text{ pc}$.

If we assume an axially symmetric disk of gas with a uniform structure of temperature $\langle T_e \rangle$, free electron density $\langle N_e \rangle$, and radius R , with a hole in the middle of radius r . The optical depth at each point is

$$\tau_\nu \approx 0.08235 \nu^{-2.1} \langle T_e \rangle^{-1.35} \langle N_e \rangle^2 L, \quad (3)$$

where L is the path length through the ionized part of the disk to the radio emission in pc. The values in Figure 5, then, correspond to $0.08235 \langle T_e \rangle^{-1.35} \langle N_e \rangle^2 L$, which is roughly the emission measure ($\langle N_e \rangle^2 L$) times $\langle T_e \rangle^{-1.35}$ times a constant. For convenience of discussion we refer to the quantity $[0.08235 \langle T_e \rangle^{-1.35} \langle N_e \rangle^2 L]$ as $EMT^{-1.35}$. When we average the maps in Figure 5 together we find peak values of $EMT^{-1.35}$ of 10.6 to the north and 10.1 to the south. Reasonable values of T_e and N_e for the inner ionized region of a gas disk of order 100 pc in radius in a radio galaxy nucleus are 10^4 K and 500 cm^{-3} , respectively, which yield a path length of $L \approx 100 \text{ pc}$. We therefore find that entirely reasonable physical parameters fit the observed free-free optical depths.

Comparing our results to the HI absorption results of Carilli et al. (1998), we have

$$\frac{\langle N_e \rangle^2 L_e}{\langle N_{\text{HI}} \rangle L_{\text{HI}}} \approx 1.3 \times 10^{-19} f \frac{\langle T_e \rangle^{1.35}}{\langle T_s \rangle} \text{ cm}^{-3} \text{ K}^{-0.35},$$

where f is the covering factor of the neutral gas and $\langle T_s \rangle$ is the average spin temperature of the Hydrogen atoms along the line of sight. These results are reasonably consistent, as can be demonstrated by the application of Saha equation with some simplifying assumptions. For argument's sake, we assume $\langle T_e \rangle \approx \langle T_s \rangle = T$, $f = 1$, and $L_{\text{HI}} \approx 100 L_e$ (i.e. that the inner 1% of the disk is ionized). Then,

$$\frac{\langle N_e \rangle^2}{\langle N_{\text{HI}} \rangle} \approx 1.3 \times 10^{-17} T^{0.35} \text{ cm}^{-3} \text{ K}^{-0.35}.$$

If we further approximate the gas as containing only Hydrogen, then the Saha equation can be written as

$$\frac{\langle N_e \rangle^2}{\langle N_{\text{HI}} \rangle} = 2.4 \times 10^{15} T^{3/2} \exp\left(\frac{-1.58 \times 10^5 \text{ K}}{T}\right) \text{ cm}^{-3} \text{ K}^{-3/2}.$$

Equating these two expressions yields an average gas temperature of $\sim 2000 \text{ K}$.

4.2. The Core

The spectrum of the core region is already inverted at the observed frequencies above 5 GHz. The cause for the inverted spectrum of the core, therefore, seems unrelated to the ionized disk of gas. Since the core is the region most likely to have large magnetic fields and large densities of relativistic energies, we suspect that the inverted spectrum of the core is due to synchrotron self-absorption. With the same 15.4-GHz data reported here, Taylor et al. (2000) infer an upper limit to the magnetic field in the core, assuming synchrotron self-absorption, of $7 \times 10^4 \text{ Gauss}$.

4.3. Probable Cause for Onset of Recent Activity

The suggestion of a dense circumnuclear disk of gas in 0108+388 may provide further insight into some of the unique characteristics of this CSO. We speculate that instabilities in such a disk could result in periodic infall of gas, which will produce renewed apparent activity. This would simultaneously explain the extended emission 20 arcsec ($78 h^{-1}$ kpc) to the East detected by Baum et al. (1990) and the young age of the compact structure inferred by Owsianik et al. (1998) and Taylor et al. (2000).

4.4. Implications for GPS Sources In General

As the results presented here demonstrate, when a radio source's flux density is produced by a number of components, absorption on large scales is needed in order for the composite spectrum to have a sharp turnover. Synchrotron self-absorption depends on the internal conditions of the source, and these conditions will vary from one part of the source to another. Such a large-scale absorption is therefore unlikely to be due to this process. On the other hand, we have also found that the core of this particular GPS source is probably synchrotron self-absorbed. Its spectrum is already turned over at the frequency where the free-free absorption becomes significant. The implication for other, and possibly all, GPS sources is that free-free absorption is the likely cause for the high-frequency turnovers of the composite spectrum, but synchrotron self-absorption may still be important on smaller scales; the turnover of a weak core component will not contribute significantly to the integrated flux densities at low frequencies.

5. CONCLUSIONS

By extrapolating our high frequency maps, we obtained opacity maps of 0108+388 at two frequencies below the spectral turnover which strongly suggest that free-free absorption, possibly by a disk of ionized gas, is indeed the cause of the spectral turnover, and perhaps in other CSOs with a GHz-peaked spectrum. The spectra all across the map fit free-free absorption well. Reasonable values for temperature (10^4 K) and electron density (500 cm^{-3}) in a disk of order 100 pc in size fit the observed optical depths.

The spectrum of the core, though, is inverted even at our highest frequencies, probably because of synchrotron self-absorption.

The presence of a dense gas disk in 0108+388, which is also consistent with the large column densities implied by the HI absorption measurements of Carilli et al. (1998), may be related to the recent onset of activity in this object, as indicated by the age estimates by Owsianik et al. (1998) and Taylor et al. (2000). The accumulated evidence thus strongly supports the conclusions that CSOs in general are intrinsically young objects that evolve into classical kpc-scale radio galaxies, and that the radio galaxy 0108+388, in particular, is the youngest source known.

This research was aided, in part, by funding from the Dudley Observatory. This research has also made use of data from the University of Michigan Radio Astronomy Observatory which is supported by funds from the University of Michigan. We are also grateful for the friendly assistance of Vivek Dhawan and the staff at the National Radio Astronomy Observatory.

REFERENCES

- Baum, S. A., O'Dea, C. P., Murphy, D. W., & de Bruyn, A. G. 1990, *A&A*, 232, 19
- Bicknell, G. V., Dopita, M. A., & O'Dea, C. P. 1997, *ApJ*, 485, 112
- Carvalho, J. C. 1985, *MNRAS*, 215, 463
- Cawthorne, T. V., Wardle, J. F. C., Roberts, D. H., Gabuzda, D. C., & Brown, L. F. 1993, *ApJ*, 416, 496
- Carilli, C. L., Menten, K. M., Reid, M. J., Rupen, M. P., & Yun, M. S. 1998, *ApJ*, 494, 175
- Conway, J. E., Myers, S. T., Pearson, T. J., Readhead, A. C. S., Unwin, S. C., & Xu, W. 1994, *ApJ*, 425, 568
- de Kool, M. & Begelman, M. C. 1989, *Nature*, 338, 484
- de Vries, W. H., Barthel, P. D., & O'Dea, C. P. 1997, *A&A*, 321, 105
- Gopal-Krishna, Patnaik, A. R., & Steppe, H. 1983, *A&A*, 123, 107
- Hodges, M. W., Mutel, R. L., & Phillips, R. B. 1984, *AJ*, 89, 1327
- Kameno, S., Horiuchi, S., Shen, Z.-Q., Inoue, M., Kobayashi, H., Hirabayashi, H., & Murata, Y. 2000, *PASJ*, 52, 209
- Kuncic, Z., Bicknell, G. V., & Dopita, M. A. 1998, *ApJ*, 495, L35
- Mezger, P. G. & Henderson, A. P., 1967, *ApJ*, 143, 471
- Mutel, R. L., Hodges, M. W., & Phillips, R. B. 1985, *ApJ*, 290, 86
- O'Dea, C. P. 1998, *PASP*, 110, 493
- O'Dea, C. P., Baum, S. A., & Stanghellini, C. 1991, *ApJ*, 380, 66
- Owsianik, I. & Conway, J. E. 1998, *A&A*, 337, 69
- Owsianik, I., Conway, J. E., & Polatidis, A. G. 1998, *A&A*, 336, L37
- Pearson, T. J. & Readhead, A. C. S. 1988, *ApJ*, 328, 114
- Phillips, R. B. & Mutel, R. L. 1982, *A&A*, 106, 21
- Readhead, A. C. S. & Wilkinson, P. N. 1978, *ApJ*, 223, 25
- Readhead, A. C. S., Taylor, G. B., Pearson, T. J., Wilkinson, P. N. 1996, *ApJ*, 460, 634
- Shepherd, M. C., Pearson, T. J., & Taylor, G. B. 1995, *BAAS*, 26, 987
- Shepherd, M. C., Pearson, T. J., & Taylor, G. B. 1995, *BAAS*, 27, 903
- Shepherd, M. C. 1997, in *A.S.P. Conf. Ser. 125, Astronomical Data Analysis Software and Systems VI*, ed. G. Hunt & H. E. Payne, (San Francisco: ASP) 77
- Snellen, I., Tschager, W., Schilizzi, R., Röttgering, H., & Miley, G. 2000 in *Astrophysical Phenomena Revealed by Space VLBI*, ed. H. Hirabayashi, P. G. Edwards, & D. W. Murphy (Tokyo: ISAS), 79
- Spoelstra, T. A. T., Patnaik, A. R., & Gopal-Krishna 1985, *A&A*, 152, 38
- Taylor, G. B., Readhead, A. C. S., & Pearson, T. J. 1996, *ApJ*, 463, 95
- Taylor, G. B., Marr, J. M., Readhead A. C. S., & Pearson, T. J. 2000, *ApJ*, 541, 112
- van Breugel, W., Heckman, T., & Miley, G. 1984, *ApJ*, 276, 79
- Wilkinson, P. N., Polatidis, A. G., Readhead, A. C. S., Xu, W., & Pearson, T. J. 1994, *ApJ*, 432, L87

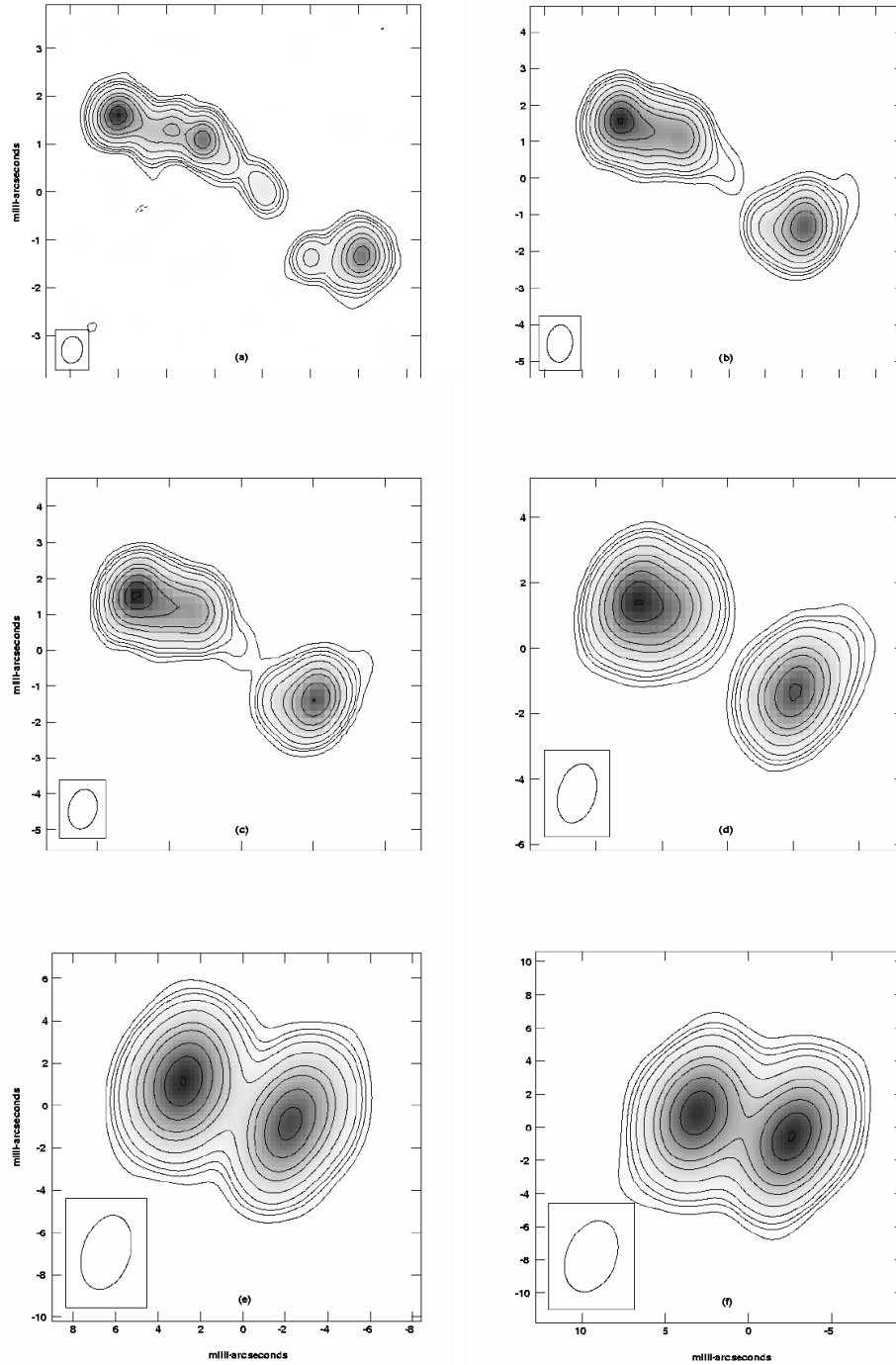


FIG. 1.— Clean maps at six frequencies and two epochs: (a) 15.4 GHz, 1997 Feb; (b) 8.4 GHz, 1997 Feb; (c) 8.4 GHz, 1996 Jun; (d) 5.0 GHz, 1996 Jun; (e) 2.3 GHz, 1996 Jun; and (f) 1.7 GHz, 1996 Jun. The displayed contours represent -3 , -2 , -1 , 1 , 2 , 3 , 5 , 10 , 20 , 30 , 50 , 75 , and 99% of the peak value. The peak values and rms noise levels are: (a) 0.1040 & 0.00033 Jy/beam; (b) 0.2228 & 0.00020 Jy/beam; (c) 0.2279 & 0.00025 Jy/beam; (d) 0.3933 & 0.00037 Jy/beam; (e) 0.3468 & 0.00069 Jy/beam; and (f) 0.2217 & 0.00069 Jy/beam. The FWHM of the clean beams (displayed in the lower left corners) are: (a) 0.56×0.44 mas, $PA = -8.6^\circ$; (b) 1.01×0.70 mas, $PA = -5.0^\circ$; (c) 1.11×0.78 mas, $PA = -13.3^\circ$; (d) 1.84×1.15 mas, $PA = -16.9^\circ$; (e) 3.61×2.22 mas, $PA = -16.7^\circ$; (f) 4.46×2.98 mas, $PA = -21.2^\circ$. The maps are not all displayed to the same scale.

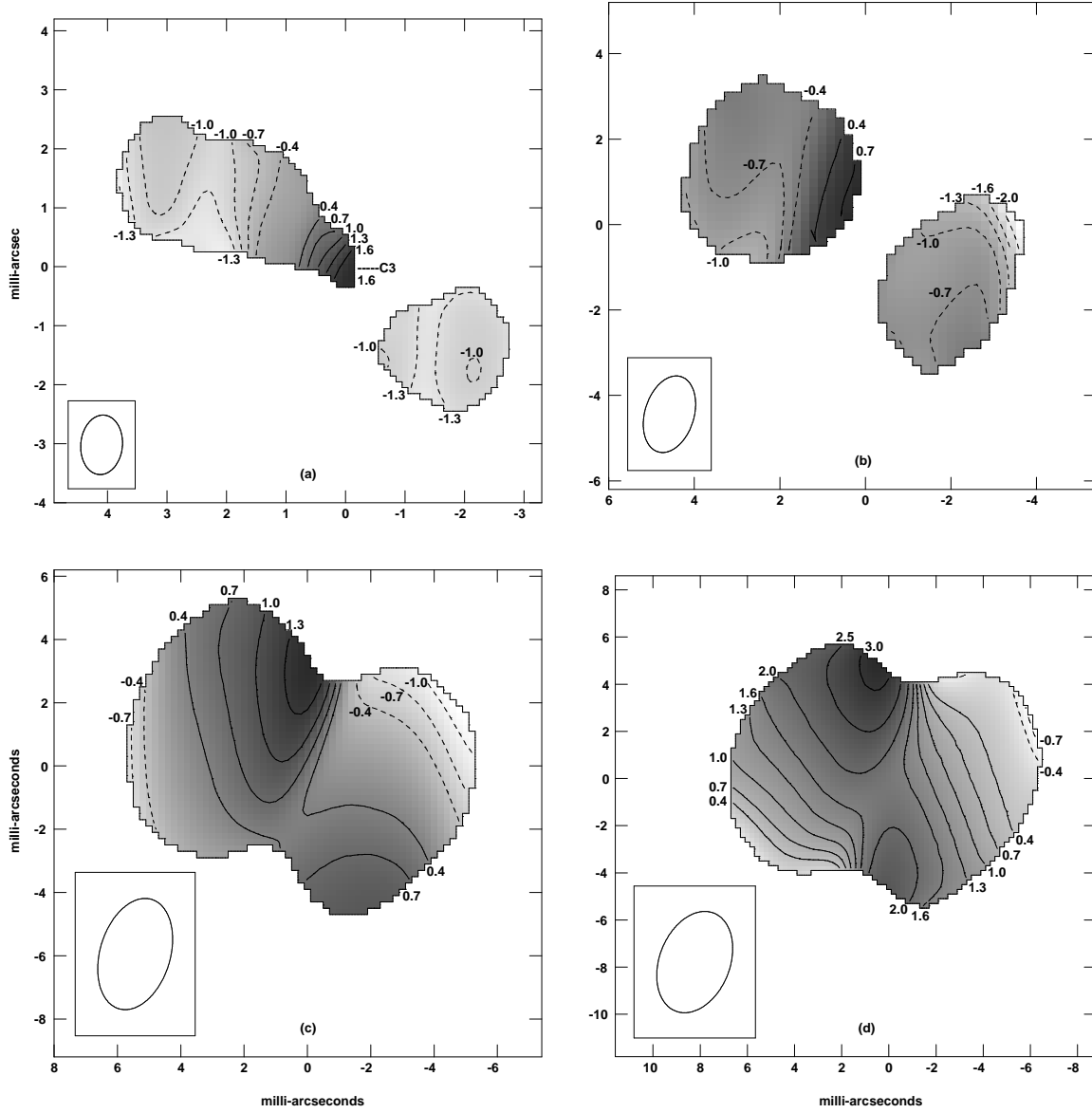


FIG. 2.— Spectral index maps: (a) between 15.4 and 8.4 GHz, 1997 Feb; (b) between 8.4 and 5.0 GHz, 1996 Jun; (c) between 5.0 and 2.3 GHz, 1996 Jun; and (d) between 2.3 and 1.7 GHz, 1996 Jun. The labels of the contours indicate spectral index values, α , where $F_\nu \propto \nu^\alpha$. Solid contours represent positive spectral indices and dashed contours represent negative spectral indices. The grey scale is darker towards larger spectral indices. The uncertainties in the spectral indices are listed in Table 1. The input clean maps were both convolved with clean beams, displayed in the lower left corners, equal to that of the lower frequency map in Figure 1. The maps are not all displayed to the same scale.

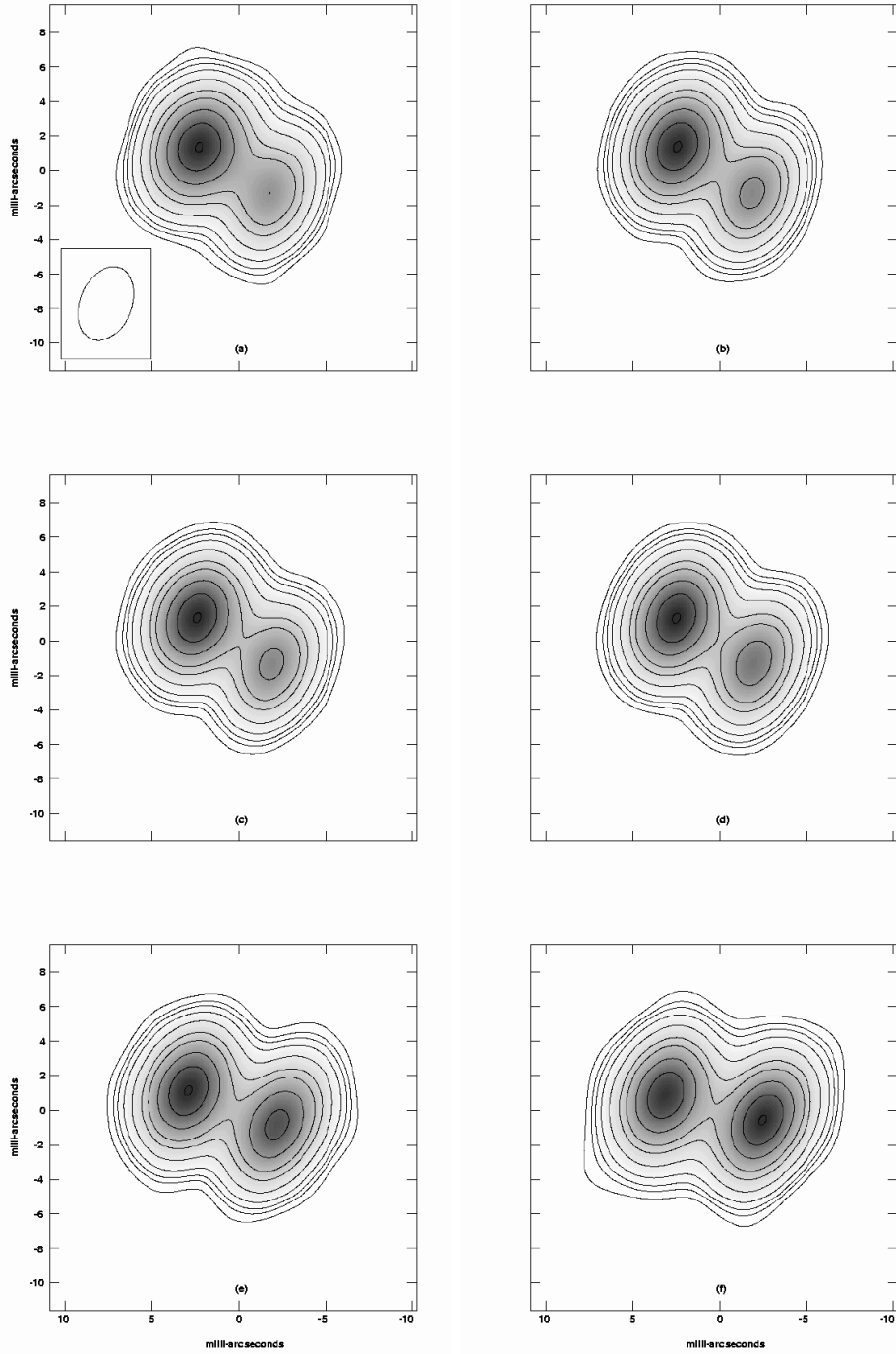


FIG. 3.— Clean maps made from truncated data sets all with the same minimum and maximum u - v distances, and convolved with the same clean beam: (a) 15 GHz, 1997 Feb; (b) 8.4 GHz, 1997 Feb; (c) 8.4 GHz, 1996 Jun; (d) 5.0 GHz, 1996 Jun; (e) 2.3 GHz, 1996 Jun; and (f) 1.7 GHz, 1996 Jun. The displayed contours represent -3 , -2 , -1 , 1 , 2 , 3 , 5 , 10 , 20 , 30 , 50 , 75 , and 99% of the peak value. The peak values and rms noise levels are: (a) 0.2713 & 0.00069 Jy/beam; (b) 0.4738 & 0.00054 Jy/beam; (c) 0.4617 & 0.00028 Jy/beam; (d) 0.6218 & 0.00036 Jy/beam; (e) 0.3788 & 0.00054 Jy/beam; and (f) 0.2212 & 0.00063 Jy/beam. The FWHM of the clean beam, which is the same for all images and is displayed in the lower left corner of figure (a), is 4.44×2.97 mas at position angle -21.5° . The maps are displayed to the same scale.

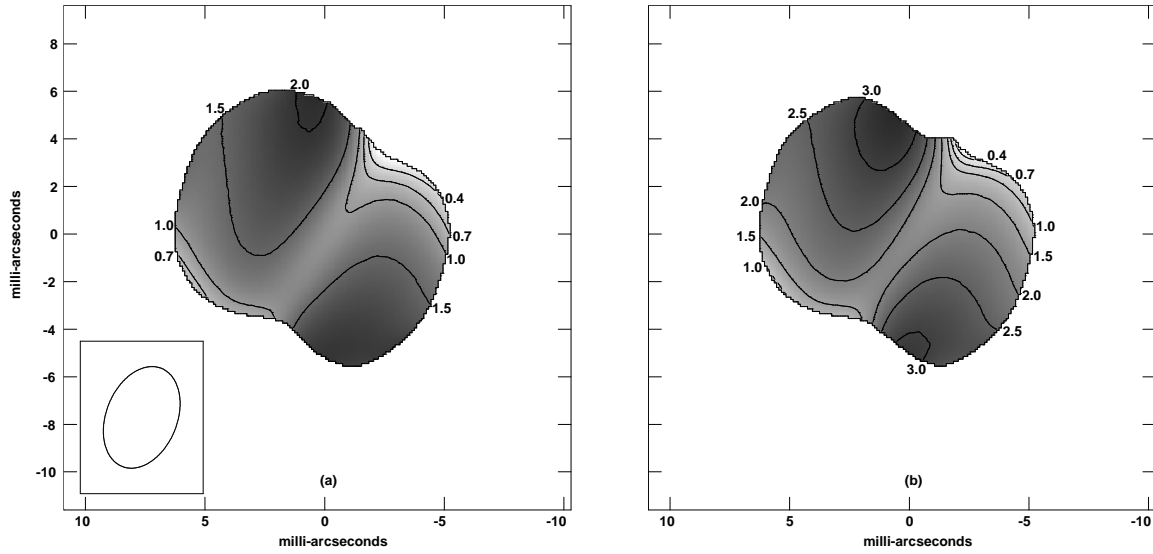


FIG. 4.— Opacity maps, made from data sets edited to yield the same resolution, at (a) 2.3 GHz and (b) 1.7 GHz. The labels of the contours indicate optical depth values with the grey scale becoming darker towards larger optical depths. The uncertainties in the optical depths are listed in Table 2.

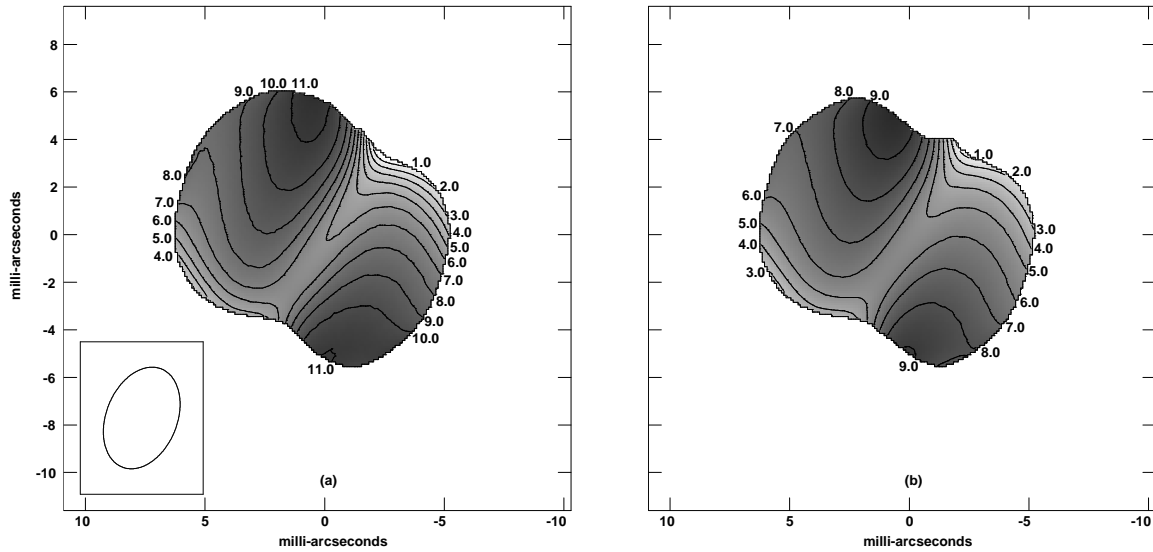


FIG. 5.— Maps of the quantity $0.08235 \int T_e^{-1.35} N_e^2 dl$ at (a) 2.3 and (b) 1.7 GHz. The uncertainties are listed in Table 2.

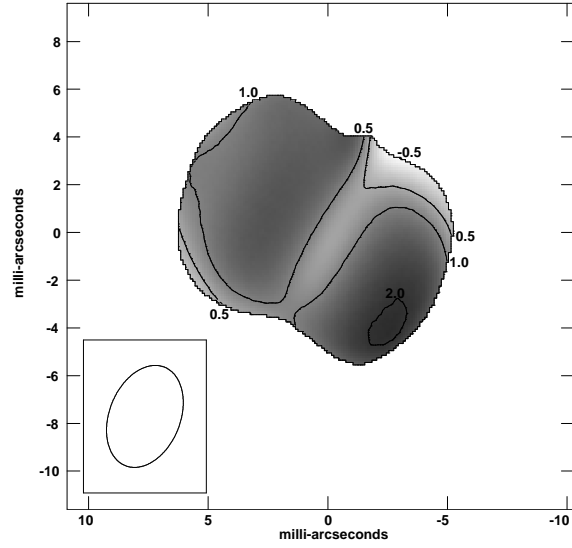


FIG. 6.— The difference between the maps in Figures 5(a) and 5(b) divided by the calculated uncertainties in this difference. The contours represent difference values of -0.5 , 0.5 , 1 , and 2 times the uncertainty.

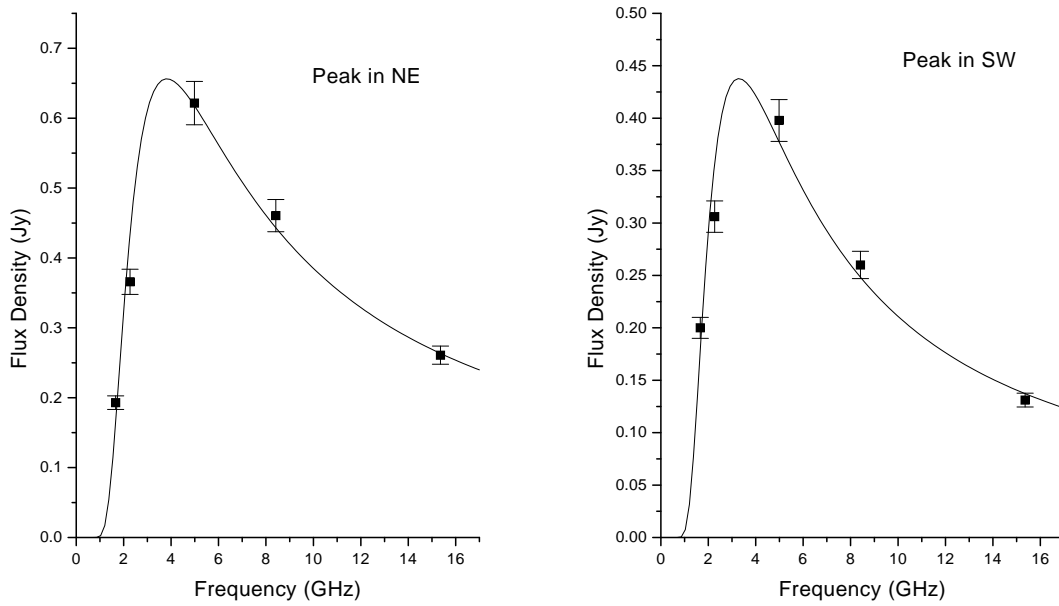


FIG. 7.— Spectra at the peaks in emission at 5.0 GHz. The error bars represent the total uncertainties in the flux densities. Overlaid as continuous lines are the best-fit curves of free-free absorption by single components in the foreground of a transparent synchrotron source.

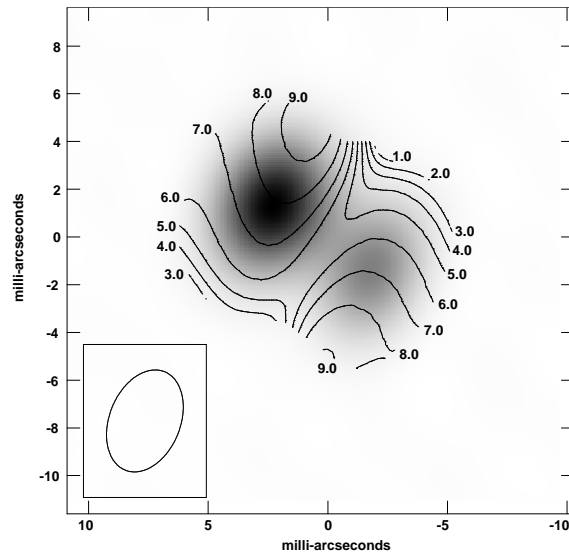


FIG. 8.— Contours from Figure 5(b) overlaid on a grey-scale plot of the emission at 15.4 GHz, as displayed in Figure 3(a).

TABLE 1

UNCERTAINTIES IN SPECTRAL INDEX MAPS DUE TO UNCERTAINTIES IN THE OBSERVED FLUX DENSITIES. UNCERTAINTIES IN OBSERVED FLUX DENSITIES RESULT BOTH FROM POSSIBLE ERRORS IN THE AMPLITUDE CALIBRATION AND FROM MAP NOISE. THE UNCERTAINTIES IN α DUE TO AMPLITUDE CALIBRATION ERRORS, LISTED IN COLUMN 2, ARE CONSTANT ACROSS EACH MAP. THE UNCERTAINTIES IN α DUE TO MAP NOISE VARIES AND DEPENDS ON THE RATIO OF THE OBSERVED FLUX DENSITY TO THE MAP RMS. SINCE THE SPECTRAL INDEX MAPS WERE TRUNCATED WHERE THE MAP SIGNALS WERE $< 10\sigma$, THE MAXIMUM UNCERTAINTY DUE TO MAP NOISE, WHICH OCCURS AT THE EDGES OF THE SOURCE, ARE CALCULATED AND ARE LISTED IN COLUMN 3.

Frequencies (GHz)	$\Delta\alpha$ due to amp. cal. errors	Max. $\Delta\alpha$ due to map noise
15.359-8.417	0.12	0.24
8.417-4.983	0.13	0.26
4.983-2.267	0.090	0.18
2.267-1.663	0.23	0.46

TABLE 2

UNCERTAINTIES IN OPTICAL DEPTHS AND IN $EMT^{-1.35}$ BASED ON 5% UNCERTAINTY IN AMPLITUDE CALIBRATION OF THE u - v DATA.

Frequency (GHz)	$\Delta\tau$	$\Delta EMT^{-1.35}$
1.663	0.21	0.60
2.267	0.17	0.96

TABLE 3

BEST FIT VALUES OF THE PARAMETERS IN A SIMPLE FREE-FREE ABSORPTION MODEL TO THE OBSERVED FLUX DENSITIES AT THE PEAKS IN THE 5.0-GHz EMISSION. THE PARAMETERS F_o , α , AND EMT ARE GIVEN IN THE MODEL BY $F_\nu = F_o(\nu/1.5359\text{GHz})^\alpha \exp(-EMT/\nu^{2.1})$. THE PARAMETER F_o WAS CONSTRAINED (SEE TEXT) WHILE THE OTHER TWO PARAMETERS WERE ALLOWED TO VARY FREELY.

Parameters	NE peak	SW peak
F_o	0.27 ± 0.03	0.14 ± 0.015
α	-0.97 ± 0.06	-1.07 ± 0.07
EMT	7.7 ± 0.8	6.2 ± 0.6
χ_ν^2	7.5	6.1